Deformation and Microstructure Evolution in Co-Ni-Cr-Mo Superalloy during Hot Working

IKA KARTIKA, H. MATSUMOTO, and A. CHIBA

Deformation and microstructure evolution in Co-33Ni-20Cr-10Mo superalloy during hot deformation are studied by carrying out compression tests between 950 °C and 1200 °C with an increment of 50 °C at strain rates of 0.1, 1, 10, and 30 s^{-1}. The flow curves obtained for the aforementioned strain rates in this temperature range show that this alloy has high work-hardening characteristics; this is due to the strong dislocation-solute interactions associated with dynamic strain aging (DSA). Microstructures deformed at temperatures up to 1050 °C consist of numerous deformation twins and highly dense dislocations, which are attributed to the high activation energy for deformation and the relatively low strain-rate sensitivity m in the temperature range of 950 °C to 1200 °C. Dynamic recrystallization (DRX), which is dependent on the strain rate, occurs at T = 1000 °C, 1050 °C, 1100 °C, 1150 °C, and 1200 °C.

I. INTRODUCTION

COBALT-BASE superalloys generally show good wear and corrosion resistance and have excellent high-temperature strength. Most of the properties of these superalloys are attributable to the crystallographic nature of cobalt (in particular, its response to stress); the solid solution strengthening effects of chromium, tungsten, and molybdenum; and the corrosion resistance imparted by chromium. High nickel content in such alloys is known to increase the stacking-fault energy (SFE) and enhance forgeability. Low SFE is often considered detrimental to hot workability, because it decreases the ability of the alloy to cross-slip and thus inhibits its recovery.[1]

As observed in a previous study, the Co-30Ni-21Cr-10Mo superalloy has a high work-hardening rate both at room temperature and elevated temperatures, where dynamic strain aging (DSA) occurs.[2] According to that study, in the DSA temperature range (500 °C to 727 °C), Suzuki segregation occurs at stacking faults bounded by Shockley partials; subsequently, dislocation dissociation is extended and cross-slip is restricted. In the present study, DSA is thought to be responsible for the high work-hardening rate of the superalloy and deformation twinning at elevated temperatures.

Deformation twins in most crystal structures are nucleated and grow readily with a decrease in the deformation temperature or an increase in the deformation rate. Deformation twinning is rarely observed in face-centered-cubic (fcc) metals, especially in those with medium or high SFE, such as copper, nickel, and aluminum.[3,4]

Deformation twinning is characterized by nucleation, intersection, and effective shear, with several degrees of freedom.[5] Studies on single crystals have revealed that twinning plays an important role in the propagation of dynamic recrystallization (DRX), particularly in alloys with low SFE.[6]

At high temperatures, usually above 0.7 T_m, and at high strain rates, many metals and alloys undergo DRX, which plays an important role in hot working by facilitating grain refinement and homogenization of structures. The DRX is exemplified by the unusual stress-strain curves obtained. At high strain rates, DRX is initiated after the peak stress is reached, after which it proceed continuously; this leads to continuous flow softening. At low strain rates, DRX is initiated before the peak strain is reached, but thereafter becomes discontinuous.[7]

However, no systematic study has been carried out on microstructural evolution in Co-33Ni-20Cr-10Mo during hot working. The objective of this research is to study the microstructural evolution in this superalloy under different hot working conditions by optical microscopy, electron backscattering diffraction (EBSD), and transmission electron microscopy (TEM) and to determine the influence of hot working parameters such as strain rate and temperature on the microstructure.

II. EXPERIMENTAL PROCEDURES

The chemical composition of the present superalloy is shown in Table I. The plate specimens used for hot compression tests were cut into cylindrical shapes (diameter: 8 mm diameter; height: 12 mm) using an electrodischarge machine (EDM) and then ground with a grinding paper (grade 3000). The cylindrical specimens were subsequently annealed at 1050 °C for 12 hours to

IKA KARTIKA, Researcher, H. MATSUMOTO, Assistant Professor, and A. CHIBA, Professor, are with the Institute of Materials Research, Tohoku University, Sendai 980-8577, Japan. Contact e-mail: a.chiba@imr.tohoku.ac.jp

obtain homogenized microstructures, which were then examined by X-ray diffraction (XRD).

A graphite foil sprayed with boron nitride was used as a lubricant to minimize the friction between the specimen and the anvils. Compression tests were carried out in vacuum from 950 °C to 1200 °C at intervals of 50 °C in a computer-aided hot-forging simulator (Thermec-master-Z). The stroke rate was set to 1.2 mm/s. A heating rate of 5 °C/s was achieved by induction heating from room temperature to the required temperatures. The sample was maintained at the temperature for 300 seconds before being subjected to compression. The sample was compressed to the final strain level and then cooled to room temperature (cooling rate: ~50 °C/s) using a mixture of N_2 (6 MPa) and He (4 MPa). The strain rates ($\dot{\varepsilon}$) chosen were 0.1, 1, 10, and 30 s^{-1}.

The samples were electropolished at room temperature at an operating voltage of 20 V using a solution of 10 pct H_2SO_4 and 90 pct CH_3OH. Then, the center of the sample, which was parallel to the longitudinal compression axis, was observed under an optical microscope. The misorientation between the new and original grains was determined using EBSD. Microstructures formed after the compression tests were observed using a transmission electron microscope (JEOL* 2000 EX;

*JEOL is a trademark of Japan Electron Optics Ltd., Tokyo.

acceleration voltage: 200 kV). The samples were cut into thin discs (thickness: approximately 1 mm) by positioning of the EDM at the center of the sample and aligning it parallel to the longitudinal compression axis; these discs were then mechanically polished to an thickness of ~0.1 mm using a grinding paper (grade 3000). The discs were further ground to a thickness of approximately 40 μm using a dimple machine. Finally, thin foils for TEM observations were obtained by subjecting the discs to ion beam milling (Gatan M691, Gatan Inc., Pleasanton, CA; 3 keV).

III. RESULTS AND DISCUSSION

A. Microstructure after Homogenization

Figure 1 shows the optical micrograph of the present superalloy after homogenization. The microstructure contains equiaxed grains and numerous annealing twins with an average grain size of approximately 116 μm. The XRD images in Figure 2 reveal five well-defined diffraction peaks with 2θ ranging from 40 to 100 deg, indicating that the microstructure comprises only the γ phase with fcc grains.

Table I. Chemical Composition of Cobalt-Base Superalloy Was Used as Specimen

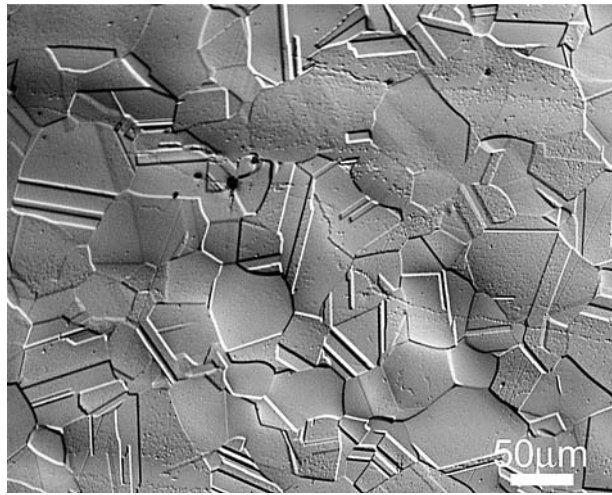| Element	Co	Ni	Cr	Mo	Mn	Nb	Fe	Ti
(Pct mass)	bal	32.9	20.1	10.1	0.28	1.04	1.79	0.44

Fig. 1—Co-33Ni-20Cr-10Mo superalloy after homogenized at $T = 1050$ °C for 12 h.
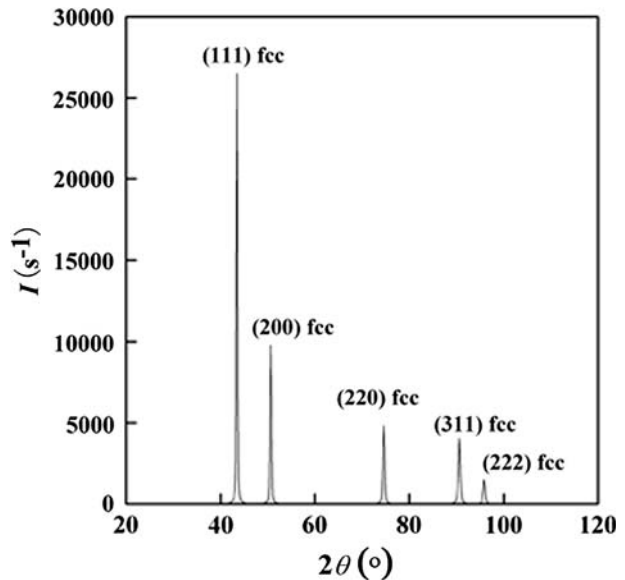

Fig. 2—XRD pattern of Co-33Ni-20Cr-10Mo superalloy after homogenization.

B. Characteristics of Deformation Behavior in True Stress/True Strain Curves

The true stress/true strain curves obtained between 950 °C and 1200 °C and at a strain of 0.5 are shown in Figures 3(a) through (f). The flow curves show significant work-hardening characteristics immediately after the yield point, particularly in the range 950 °C to 1050 °C, irrespective of the strain rate. Yield drop and moderate work hardening occur at 1100 °C and 1150 °C at a strain rate of 0.1 s^{-1} and at 1200 °C at strain rates of 0.1 and 1 s^{-1}. Note that the yield drop phenomenon is associated with the subsequent moderate work hardening; if no yield drop occurs, significant work hardening will be observed immediately after the yield point. Generally, yield drop occurs if the density of the mobile
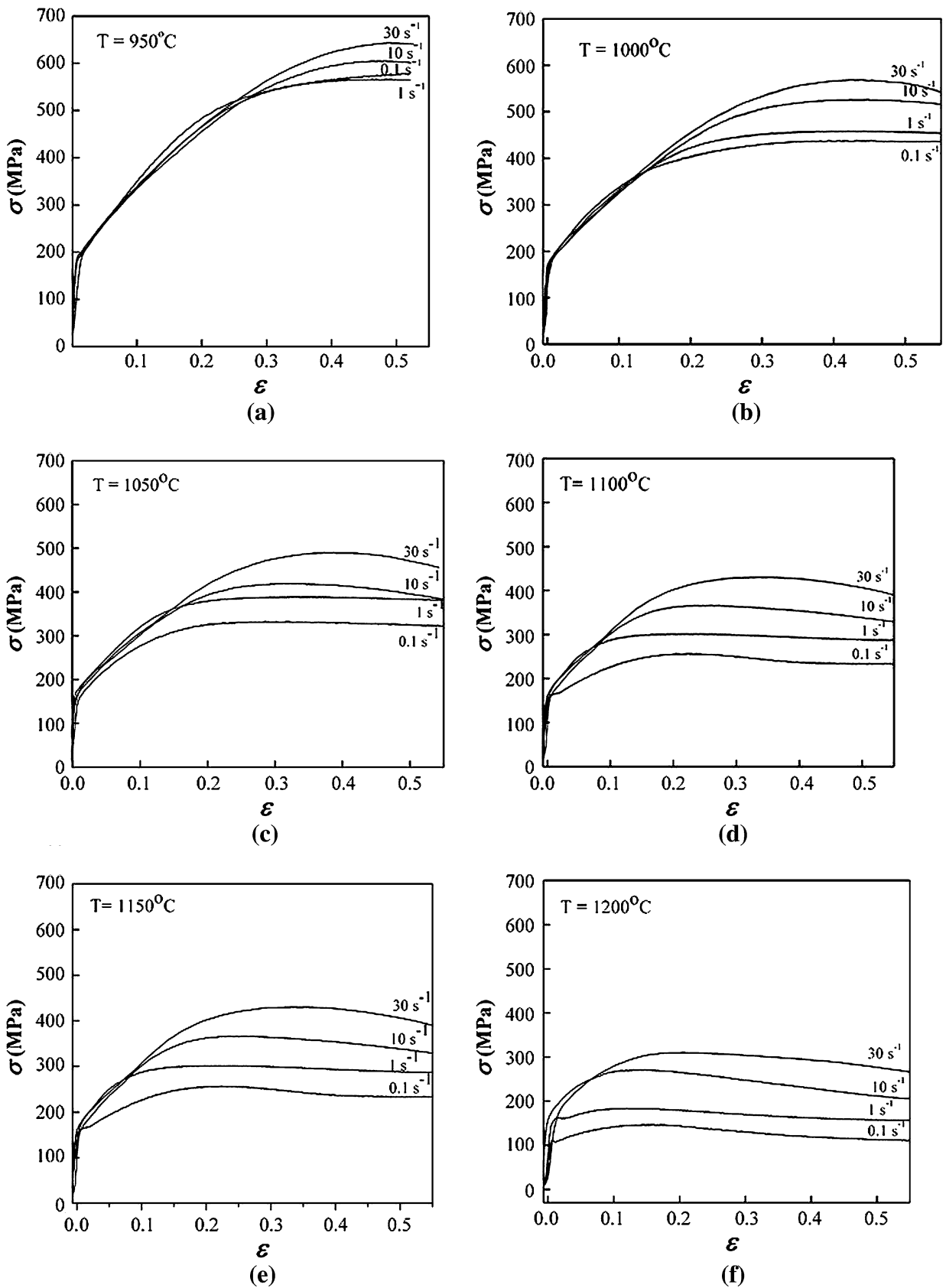
Fig. 3—True stress–true strain curves of Co-33Ni-20Cr-10Mo superalloy obtained from load displacement data at $\dot{\varepsilon} = 0.1$ to 30 s^{-1}, at T (°C): (a) 950, (b) 1000, (c) 1050, (d) 1100, (e) 1150, and (f) 1200.

dislocations increases abruptly at the yield point. In the present superalloy, residual and multiple dislocations formed during straining are thought to be immobilized between 950 °C and 1000 °C (Figures 3(a) and (b)). On the other hand, when the temperature is increased, these immobilized residual dislocations abruptly become mobile just before the yield point, and subsequently the large number of dislocations formed during the viscous motion.

In fcc metals, the yield stress is strongly dependent on the strain rate and temperature.[13] On the basis of a thermally activated dislocation glide, it is proposed that the yield stress generally increases with the strain rate. However, this relation does not hold well for the present superalloy. From the plot of yield stress vs logarithmic strain rate shown in Figure 4, it is apparent that, between 950 °C and 1000 °C, the yield stress does not increase but decreases with an increase in the strain rate. Thus, it is found that the yield stress shows a negative strain-rate sensitivity m, i.e., $m < 0$. The negative value of m is mostly due to DSA.[2] It has been well established[8] that DSA results from diffusion of the solute into the dislocations during plastic deformation in a susceptible temperature range. The DSA brings about a drastic decrease in the dislocation mobility, and this decrease is usually more effective within a limited range of strain rates.[9] This indicates that, between 950 °C and 1000 °C, yielding is not dominated by the thermally activated dislocation glide. It should be emphasized that the dislocation-solute interactions–DSA strongly affects the hot-deformation behavior, particularly in the range 950 °C to 1000 °C. Between 1050 °C and 1200 °C and at all strain rates, the yielding characteristics are similar to those observed for common fcc metals and are dominated by the thermally activated dislocation glide. However, unlike those formed in ordinary fcc alloys, dislocations (particularly residual dislocations) in the present superalloy are immobilized by the solute molecules before the yield point. Thus, the observed yield drop is due to the unpinning of the dislocations
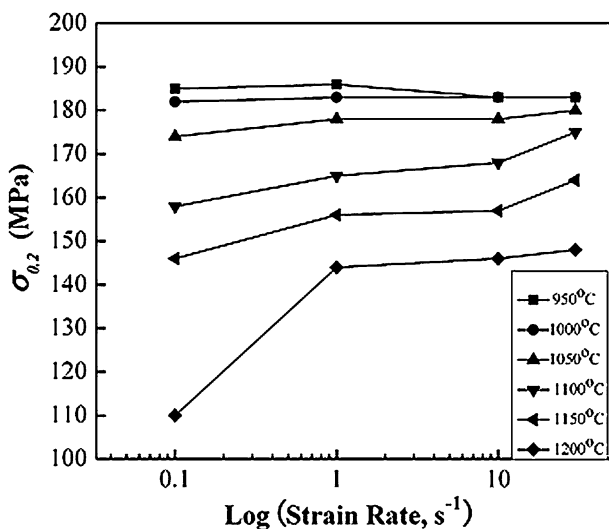
immobilized by the solute molecules surrounding the residual dislocations.

Guimaraes and Jonas[12] have reported the occurrence of the yield drop phenomenon in nickel-base superalloys during hot deformation of IN-100,[10] IN 17,[11,12] and Waspaloy.[12] They attributed the yield drop in the solution-heat-treated Waspaloy tested above the γ' solvus to the short-range-order locking of the dislocations. Another possible mechanism underlying the yield drop is dislocation pinning by fine particles,[13] which are most likely to be γ' and fine carbides in the case of superalloys.

1. Compensation for Friction and Adiabatic Heating

The following relation[14,15] was used to analyze the compensation for friction during hot working, which affects the flow stresses obtained from the load displacement data.

$$\sigma = C^2 P / 2[\exp(C) - C - 1] \qquad [1]$$

with

$$C = 2\mu(r/h)$$

In Eq. [1], σ is the stress in the absence of friction; P, the flow stress of the material under friction; r, the radius of the sample; h, the sample height; and μ, the friction coefficient determined from the barreling factor for each specimen.

In fact, after lubrication, the surface roughness changes the friction and the extent of barreling or misalignment. The friction between the workpiece and the anvil exists throughout the experiment and is an issue that remains to be solved before further use. The friction correction is carried out when P and μ are substituted into Eq. [2]. To compensate for μ, the following relationship has been proposed:[16]

$$\mu = (R/h) \cdot \frac{b}{[4/\sqrt{3} - 2b/3\sqrt{3}]} \qquad [2]$$

with

$$b = 4(\Delta R / R) \cdot (h / \Delta h)$$

Here, b is the barreling factor; ΔR, the difference between the maximum radius R_m and the top radius R_t of the specimen; R, the hypothetical frictionless radius of the specimen after deformation (determined by assuming that the specimen has a constant volume); h, the final height; and Δh, the difference between the initial and final heights of the sample.

The increase in temperature caused by adiabatic heating during deformation is usually calculated from the following equation:[14,15]

$$\Delta T = \eta / \rho c \int_0^\varepsilon \sigma \cdot d\varepsilon \qquad [3]$$

Fig. 4—Variation in $\sigma_{0.2}$ of Co-33Ni-20Cr-10Mo superalloy at various T (°C) as a function of $\dot{\varepsilon}$.

Here, η is the efficiency of deformation heating; ρ, the density; and c, the heat capacity.

Figures 5(a) through (f) show the true stress/true strain curves obtained after the compensation for friction and adiabatic heating. In contrast to flow stresses obtained from load displacement data (Figure 3), the stress peaks here disappear from the true stress/true strain curves at 950 °C to 1050 °C (Figures 5(a) through (c)). All the curves show work-hardened characteristics in the experimental strain range. These results are attributed to the elimination of the effect of the increase in adiabatic temperature during deformation by compensation for μ. Furthermore, the pronounced yield drop observed in the raw data is not observed after the compensation; therefore, the stress peaks are not clearly observed after the compensation. However, these are due to the compensation procedure and are not actual material effects; the stress-strain data used in the calculations of compensation for friction and adiabatic heating use a strain interval of 0.025.

2. Analysis of True Stress/True Strain Curves after Compensation

The dependence σ on temperature (T) and $\dot{\varepsilon}$ during high-temperature deformation can be expressed using the following power-law equation:[14]

$$\sigma = A(\dot{\varepsilon})^m \exp(mQ/RT) \qquad [4]$$

where A is an empirical constant; m, the strain-rate sensitivity; and Q, the activation energy for deformation. The value of m at constant strain and temperature can be estimated by the following equation:

$$m = \delta \ln \sigma / \delta \ln \dot{\varepsilon} \qquad [5]$$

If the steady-state flow or flow peaks specifically appearing during DRX are considered, the condition of constant strain need not be considered in the estimation of m in Eq. [5].

Then, Q can be estimated using the following equation:

$$Q = R/m\left(\frac{\delta \ln \sigma}{\delta 1/T}\right) \qquad [6]$$

Here, m, the slope of the plot of $\ln \sigma$ vs $\ln \dot{\varepsilon}$ from Eq. [5], and Q from Eq. [6] can be obtained graphically from the data plots of $\ln \sigma$ vs $\ln \dot{\varepsilon}$ and $\ln \sigma$ vs $1/T$, respectively. To apply the power-law equation for hot deformation, the following two assumptions are made: (1) m is independent of the strain rate, although it can be a function of T; and (2) Q is independent of T, although it may depend on the strain rate or flow stress.

Figures 6(a) and (b) show the variation in $\ln \sigma_{peak}$ vs $\ln \dot{\varepsilon}$ and $\ln \sigma_{peak}$ vs $1/T$ calculated using Eqs. [5] and [6], respectively. The peak stresses are used from the data illustrated in Figure 5. It should be noted that the flow curves obtained in the range of 950 °C to 1050 °C show work-hardening characteristics at all strain rates. Hence, the flow stresses at a strain of 0.5 ($\sigma_{0.5}$) are considered to be the peak stresses. Therefore, the plots with arrow marks in Figures 6(a) and (b) indicate the work-hardened stresses. Nevertheless, good linear fitting is

obtained when using all the data points in the figures. The results indicate that the two assumptions mentioned previously are valid at all strain rates and temperatures.

The variations in $\ln \sigma_{0.5}$ vs $\ln \dot{\varepsilon}$ and $\ln \sigma_{0.5}$ vs $1/T$, where steady-state flow occurs except at 950 °C and 1000 °C, are indicated in Figures 7(a) and (b), respectively. Similarly, all the data points are well fitted by linear regression, indicating that the two assumptions mentioned previously are valid at all strain rates and temperatures. The m values for σ_{peak} and $\sigma_{0.5}$ are estimated from the slope of the linear fitting of $\ln \sigma$ vs $\ln \dot{\varepsilon}$ and are tabulated in Tables II and III.

It is found that m has a small value in the temperature range from 950 °C to 1050 °C (Tables II and III), suggesting that the effect of DSA[2] still exists. Van den Beukel and Kocks[17] have reported that the mobility of a solute makes a negative contribution to the total value of m and that this contribution increases with the strain; when the total value of m becomes negative, plastic flow becomes unstable and becomes jerky flow (Portein–Le Chatelier effect). According to Montheillet and Jonas,[18] the temperature dependency of m observed in the experimental data collected for various engineering alloys and metals is theoretically and experimentally formulated in the following equation.

$$m = \frac{0.25}{1 + 4(1/T_H - 1)}(T_H = T/T_M) \qquad [7]$$

Here, T_H is the homologous temperature defined as $T_H = T/T_M$, where T_M is the melting (or solidus) temperature. The curve of temperature dependency of m employed in Eq. [7] is illustrated in Figure 8, and the m values in Tables II and III are plotted in this figure. As shown in this figure, the data points follow the curve at high temperatures, indicating that the mechanism of hot deformation of the present superalloy is identical to that of the hot deformation of engineering alloys at high temperatures. However, m in the present superalloy shows a negative deviation from the curve when the temperature is decreased from 1050 °C to 950 °C. Thus, it is deduced that the hot deformation mechanism at high temperatures differs from that at low temperatures. Accordingly, the slope of the variation in $\ln \sigma$ vs $1/T$ in Figures 6(b) and 7(b) in the range 1100 °C to 1200 °C is used to determine Q in Eq. [6]. The results of our calculations are listed in Tables II and III. The average apparent activation energy for σ_{peak} and $\sigma_{0.5}$ are 439 and 549.6 kJ/mole, respectively.

3. Constitutive Equation for Hot Deformation

The Zener–Hollomon parameter is obtained by using the average values of Q, $Z = \dot{\varepsilon} \exp\left(\frac{Q}{RT}\right)$, for different strain rates and temperatures. The dependences of σ_{peak} and $\sigma_{0.5}$ on Z (Figures 6(c) and 7(c)) in the range of 1000 °C to 1200 °C are given as $\ln(\sigma_{peak}) = 0.470 + 0.1313 \ln(Z)$ and $\ln(\sigma_{0.5}) = -1.684 + 0.1491 \ln(Z)$, respectively. In both figures, a linear relationship is obtained between $\ln \sigma$ and $\ln Z$, with regression coefficients of 0.99 to 0.98. The data points in the low-temperature range of 950 °C to 1050 °C, which are excluded when calculating Q, are also indicated in these figures for comparison. As shown in Figure 6(c),
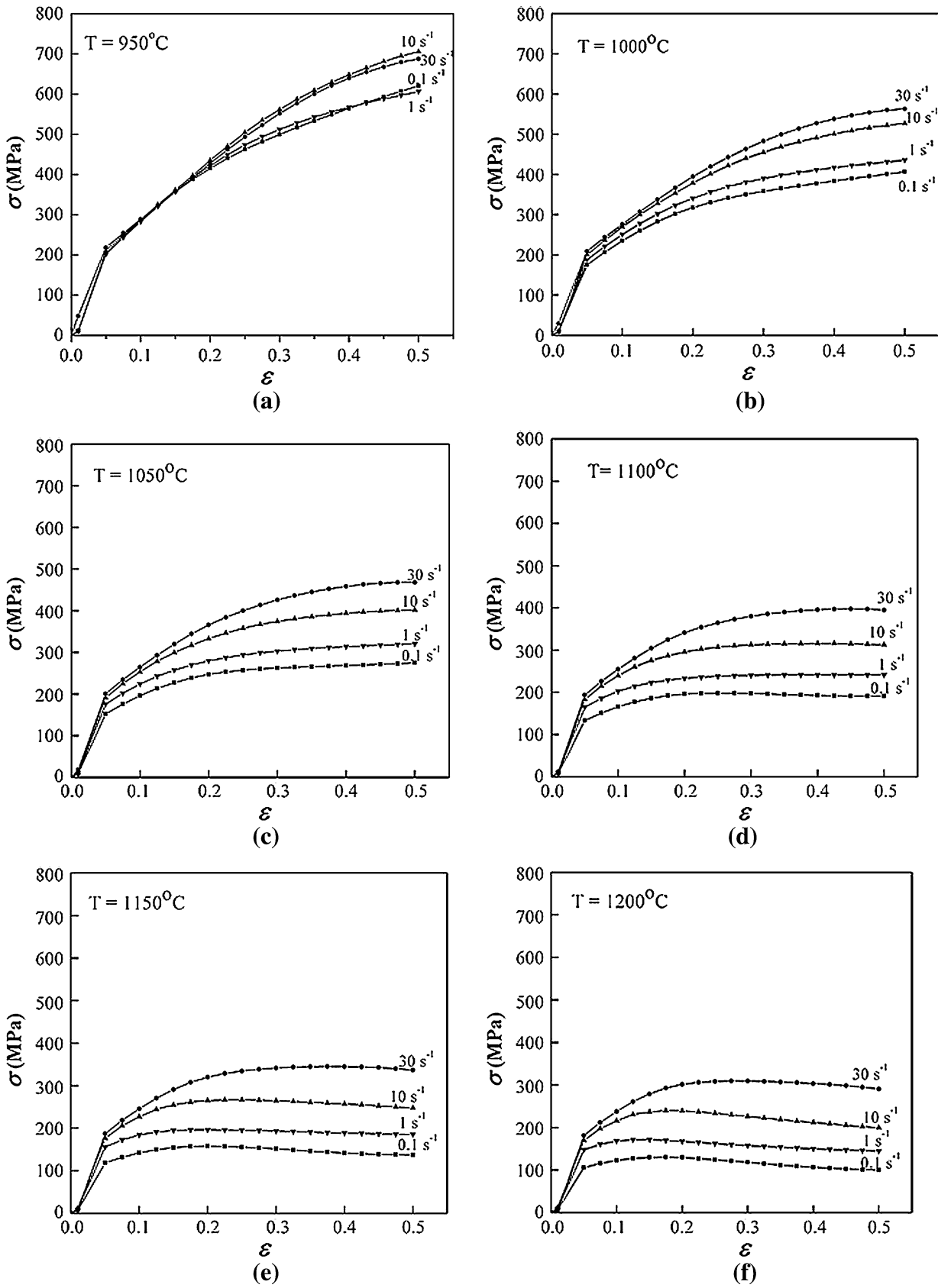
Fig. 5—True stress/true strain curves of Co-33Ni-20Cr-10Mo superalloy at $\dot{\varepsilon}$ = 0.1 to 30 s^{-1}, at T (°C): (*a*) 950, (*b*) 1000, (*c*) 1050, (*d*) 1100, (*e*) 1150, and (*f*) 1200.
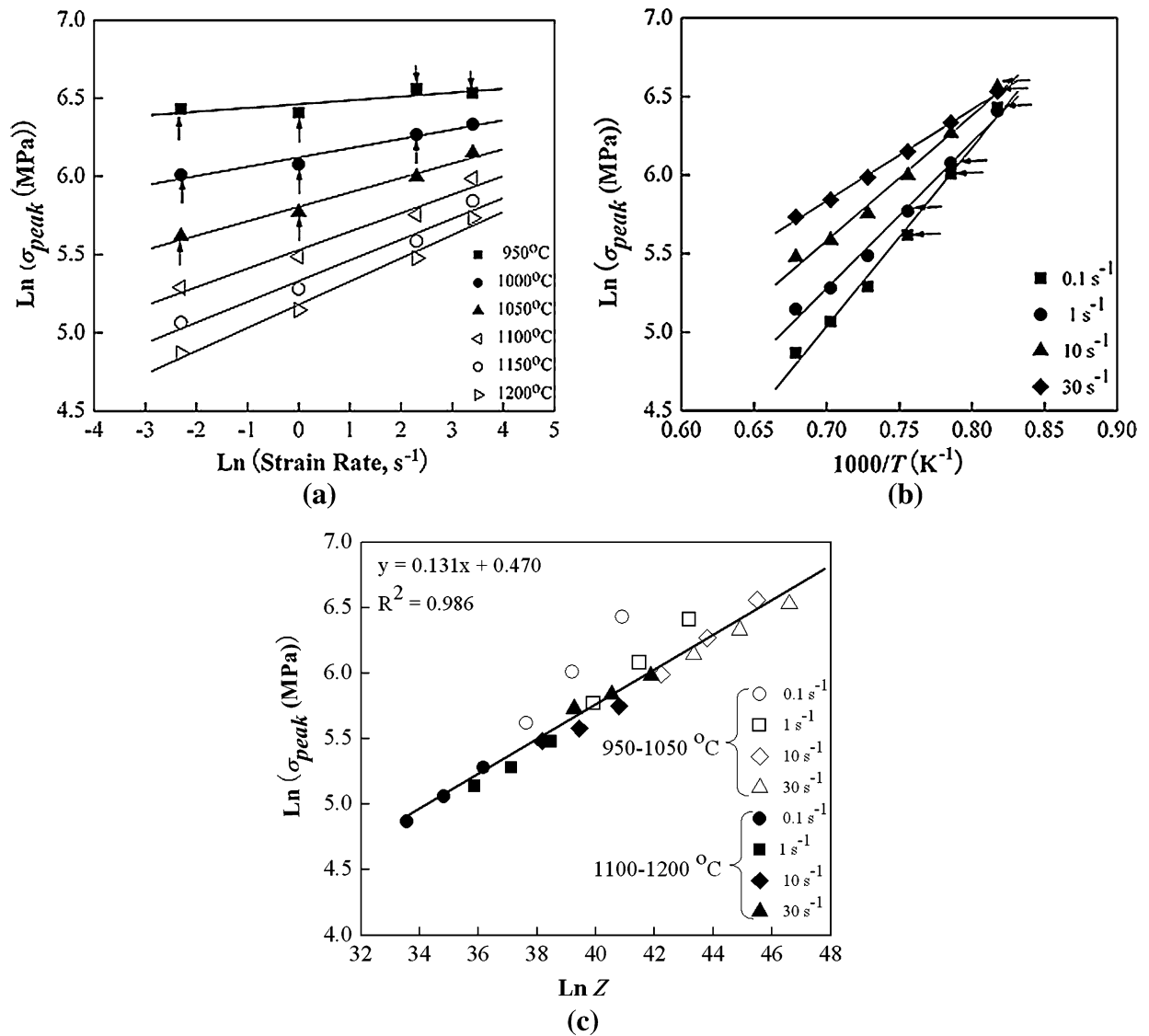
Fig. 6—Relationship between $\dot{\varepsilon}$ and σ_{peak} of Co-33Ni-20Cr-10Mo superalloy using power-law equation shows (a) ln $\dot{\varepsilon}$ vs ln σ_{peak}, (b) 1/T (K^{-1}) vs ln σ_{peak}, and (c) ln Z vs ln σ_{peak}.

the stresses at low strain rates increase with Z and deviate upward from the regression line. However, at strain rates of 30 s^{-1}, the flow stress linearly increases with the Z, thus following the regression line. This trend suggests that, in the DSA temperature range, i.e., 950 °C to 1050 °C, and at high strain rates, deformation is associated with the fact that dislocation-solute interactions decrease with an increase in the strain rate.

4. Activation Energy for Deformation (Q)

The apparent activation energies of the present superalloy in the temperature range of 1100 °C to 1200 °C, which are considered to be equal to those obtained for ordinary engineering alloys, are comparable to those reported for the deformation of superalloys, i.e., 397 kJ/mole for the hot deformation of cobalt-base superalloys,[19] 400 to 483 kJ/mole for IN718,[20–25] and 468 to 743 kJ/mol for U720 or Waspaloy.[12,26–28]

However, none of the preceding values are close to the activation energies for the self-diffusion of cobalt (286 kJ/mol), diffusion of nickel (270 kJ/mol), or diffusion of chromium (273 kJ/mol) in fcc Co.[8] For pure metals and dilute alloys, the activation energies for hot working agree with those for creep and diffusion. In addition, for alloys that undergo DRX, the activation energies for hot working are observed to be considerably larger than those proposed by any speculated atomic mechanism because of the effects of addition of solute, precipitation, dispersoid, reinforcements, and inclusions as a result of their serious retardation of the normal creep dislocation mechanisms near the bottom of the working range.[9] Thus, in engineering alloys, including the present superalloy, activation energies should be calculated on the basis of the flow curves obtained at a constant structure: dynamically recrystallized grains.
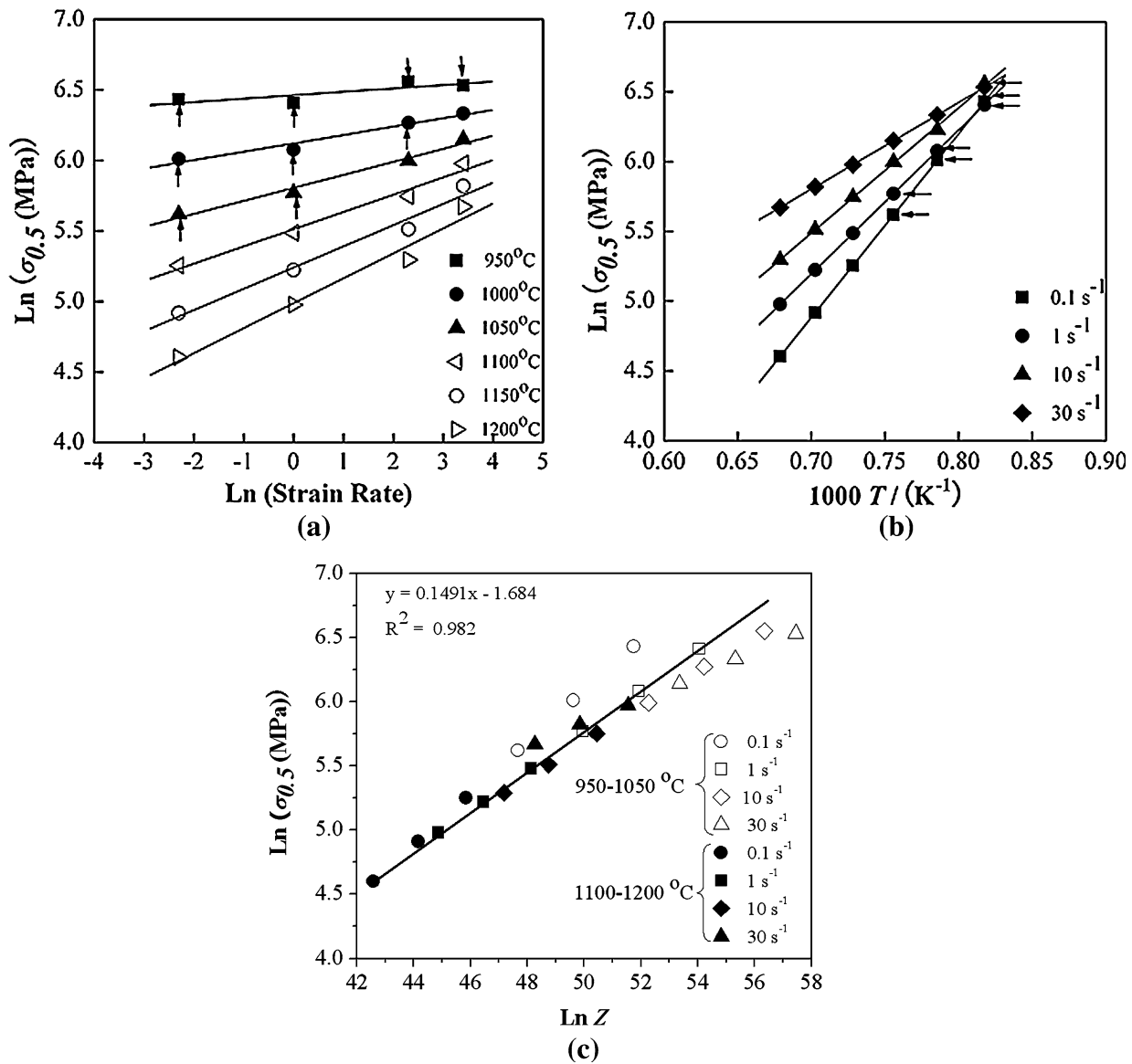
Fig. 7—Relationship between $\dot{\varepsilon}$ and $\sigma_{0.5}$ at $\varepsilon = 0.5$ of Co-33Ni-20Cr-10Mo superalloy using power-law equation shows (a) ln $\dot{\varepsilon}$ vs ln $\sigma_{0.5}$, (b) $1/T$ (K^{-1}) vs ln $\sigma_{0.5}$, and (c) ln Z vs ln $\sigma_{0.5}$.

Table II. Apparent of Activation Energy (Q) Calculated by Using the Value of m Evaluated for Peak Stress

σ_{peak}	T (°C)	950	1000	1050	1100	1150	1200
m		0.0244	0.0595	0.0922	0.119	0.133	0.148
$\dot{\varepsilon}$ (s^{-1})	$\frac{\partial \ln \sigma_{peak}}{\partial (1/T)}$			Q (kJ/mole)			
0.1	8.5323	2910	1193	770	599	535	479
1	6.920	2359	968	624	486	434	389
10	6.771	2308	947	611	475	424	380
30	5.664	1931	792	511	397	355	318

Figures 9(a) and (b) show the dependence of the Q values of the present superalloy listed in Tables II and III on temperature and strain rate. The figures show that Q increases with a decrease in the deformation temperature and strain rate. With deformation at 950 °C at strain rates ranging from 0.1 to 30 s^{-1} and at a strain of 0.5, Q becomes very high, around 4485 to 2115 kJ/mole, and the deformed microstructure comprises numerous deformation twins; further, the alloy undergoes partial DRX, and dense dislocations are

Table III. Apparent of Activation Energy (Q) Calculated By Using the Value of M Evaluated For Stress at 0.5 Strain

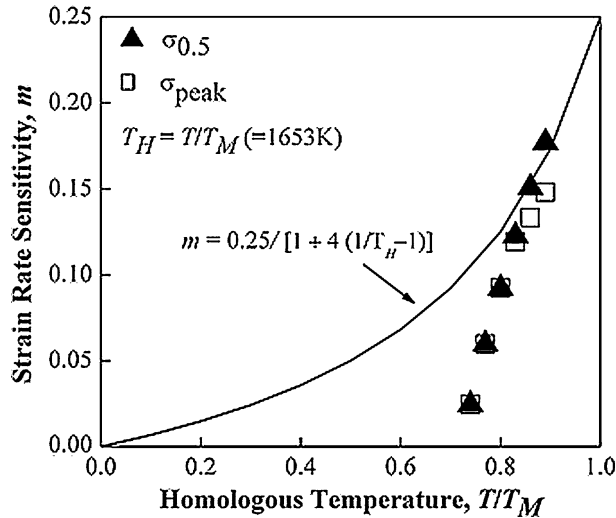| $\sigma_{0.5}$	T (°C)	950	1000	1050	1100	1150	1200
m		0.02439	0.05946	0.09215	0.1224	0.1506	0.1769
$\dot{\varepsilon}$ (s^{-1})	$\frac{\partial \ln \sigma_{0.5}}{\partial (1/T)}$			Q (kJ/mole)			
0.1	13.16	4485	1840	1187	893	726	618
1	10.31	3513	1441	930	670	569	484
10	9.105	3104	1273	822	618	502	428
30	6.206	2115	868	560	421	343	292

Fig. 8—T (°C) dependence of the m drawn by Eq. [7]. Comparison with the experimental data.
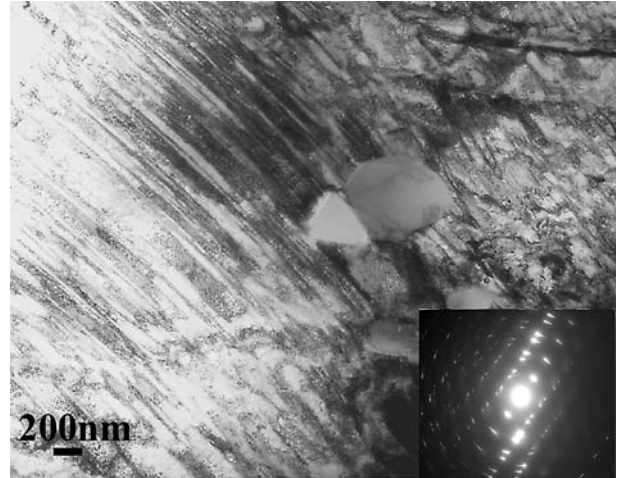

Fig. 10—TEM micrograph and diffraction pattern deformed by $\varepsilon = 0.5$ at $T = 950$ °C at $\dot{\varepsilon} = 10$ s^{-1}.
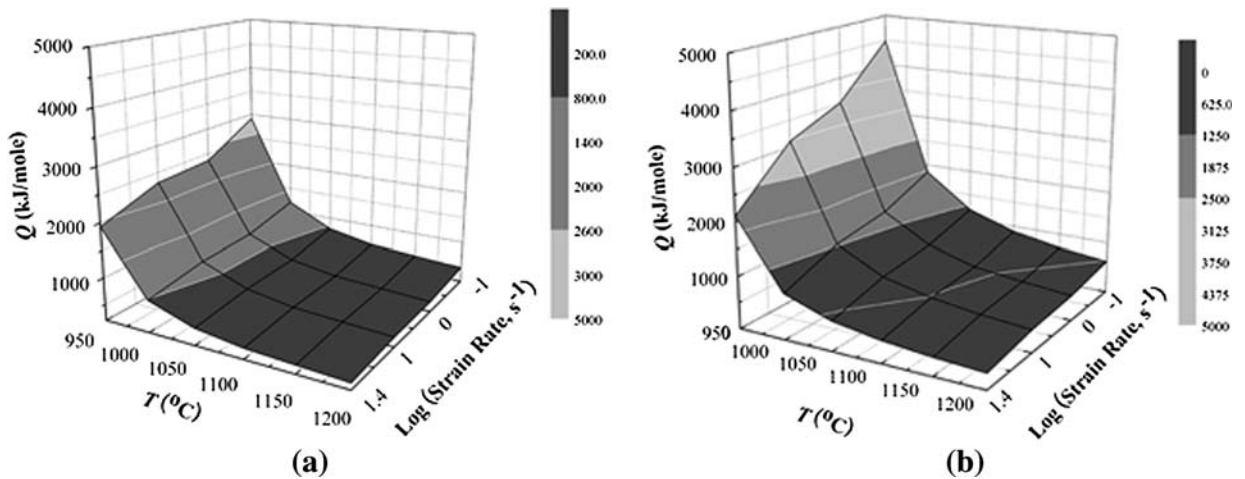

Fig. 9—T (°C) and $\dot{\varepsilon}$ (s^{-1}) dependence of apparent Q for deformation of Co-33Ni-20Cr-10Mo superalloy calculated by using m evaluated for (a) σ_{peak} and (b) $\sigma_{0.5}$.

formed (Figure 10). Therefore, the high Q values observed after deformation condition are associated with the solute-dislocation interactions–DSA or deformation twinning.

C. *Microstructure Evolution*

Figure 11 shows the optical microstructures of the present superalloy after hot compression tests at 950 °C to 1200 °C, at strain rates of 0.1 to 30 s^{-1}, and at a
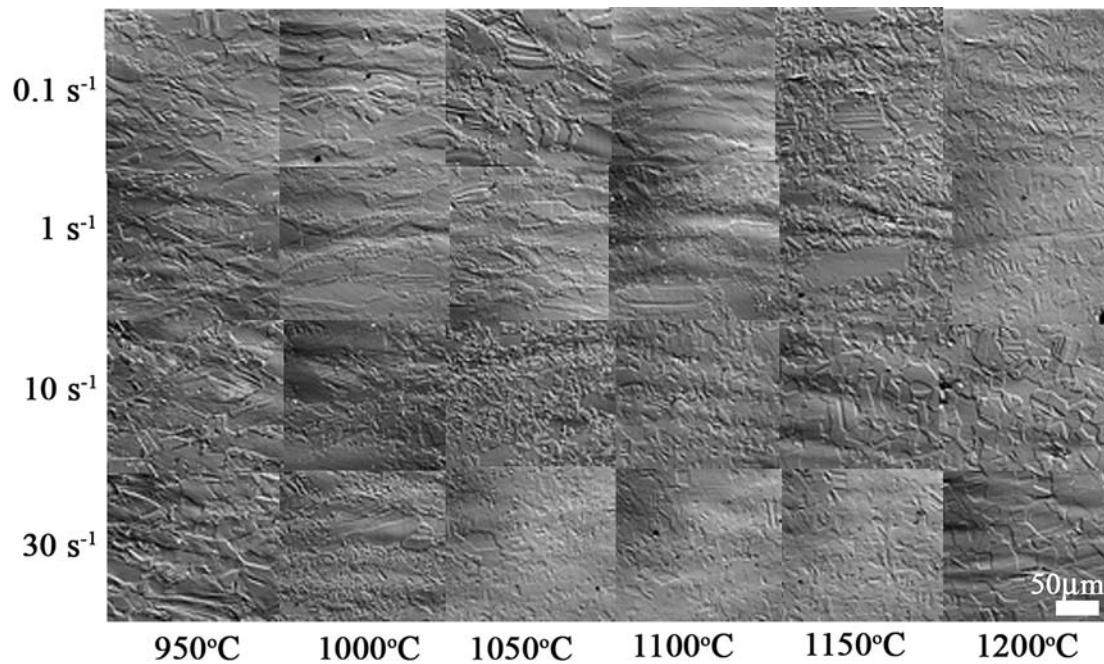
Fig. 11—Optical microstructures of Co-33Ni-20Cr-10Mo superalloy deformed at $\varepsilon = 0.5$.

strain of 0.5. It is apparent that the microstructures obtained are sensitive to the deformation temperature and strain rate.

At 950 °C and at all strain rates, the present superalloy exhibits a deformed microstructure, which consists of elongated grains with a large number of thick deformation twins and thick annealing twins. The deformed microstructure at strain rates of 10 and 30 s^{-1} consists of a greater number of deformed grains with numerous deformation twins when compared to those at lower strain rates, *i.e.*, $\dot{\varepsilon} = 0.1$ and 1 s^{-1}. Figure 10 shows the TEM micrograph of the microstructures deformed at 950 °C at a strain rate of 10 s^{-1}, corresponding to Figure 11. The images show numerous deformation twins and dense dislocations; no recovered microstructures are observed except for the new fine grains nucleating along the grain boundaries in the deformed microstructures.

At 1000 °C, at strain rates of 0.1, 1, 10, and 30 s^{-1}, deformed microstructures with new fine grains growing along the grain boundaries are clearly seen to form a so-called necklace structure. When the strain rate is increased from 10 to 30 s^{-1}, a layer of new fine grains evolves to several layers along the grain boundaries, and numerous new fine grains also form along the boundaries of the deformation twins. This indicates that the boundaries of the deformation twins can act as nucleation sites for DRX. In addition, the deformation twin areas decrease with an increase in the strain rate; these twins are replaced by new fine grains.

Similar deformed microstructures are also observed at a temperature of 1050 °C at $\dot{\varepsilon} = 0.1$ and 1 s^{-1}. However, when $\dot{\varepsilon}$ is increased to 10 and 30 s^{-1}, very fine recrystallized grains are found in the entire specimen. With a further increase in $\dot{\varepsilon}$, the grain size of the dynamically recrystallized grains increases. When $\dot{\varepsilon}$ is further increased to 30 s^{-1}, DRX occurs, and the deformation twins are replaced by dynamically recrystallized grains.

At a temperature of 1100 °C at strain rates of 0.1, 1, 10, and 30 s^{-1}, it is found that the deformed grains are surrounded by numerous fine grains along the grain boundaries. The number of deformation twins at this temperature is lesser than that at lower temperatures. When $\dot{\varepsilon}$ is increased from 10 to 30 s^{-1}, dynamically recrystallized grains completely replace the deformed microstructures.

When the temperature is increased to 1150 °C, almost 100 pct formation of dynamic recrystallized grains is observed for $\dot{\varepsilon}$ values of 0.1 and 1 s^{-1}, with the average grain sizes of 22 and 23.5 μm, respectively. On the other hand, dynamically recrystallized crystals with average grain sizes of 27 and 31 μm are formed for $\dot{\varepsilon}$ of 10 and 30 s^{-1}, respectively.

Furthermore, when the temperature is increased to 1200 °C, 100 pct DRX (grain size: 24 μm) is observed at 0.1 s^{-1}. The size of the dynamically recrystallized grains increases with $\dot{\varepsilon} = 29$ μm at $\dot{\varepsilon} = 1$ s^{-1}, 28.5 μm at $\dot{\varepsilon} = 10$ s^{-1}, and 36.5 μm at $\dot{\varepsilon} = 30$ s^{-1}. Therefore, it can be concluded that, in the temperature range in which the formation of deformation twinning is negligible, the grain size of the dynamically recrystallized grains increases with temperature and $\dot{\varepsilon}$, possibly because of nucleation sites at the deformation twin boundaries.

Figure 12(a) shows the EBSD orientation map of the microstructure deformed at 1200 °C at 0.1 s^{-1}, corresponding to the microstructure shown in Figure 11. The black line represents the high-angle (15 to 90 deg) grain boundaries. Almost all of the recrystallized grains have
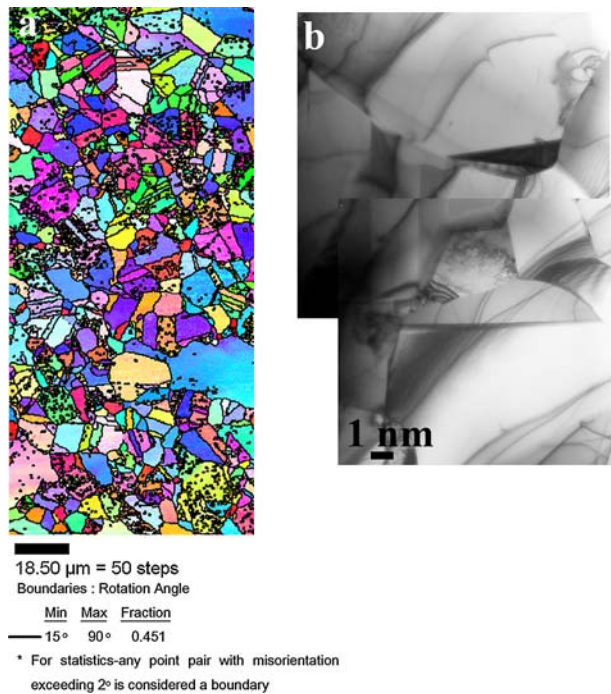
Fig. 12—(a) EBSD orientation map and (b) TEM microstructure deformed at $\varepsilon = 0.5$, $T = 1200$ °C, and at $\dot{\varepsilon} = 0.1$ s^{-1}.

high-angle grain boundaries. The TEM micrograph shown in Figure 12(b) indicates that most of the grains are free from dislocations, suggesting that the sub-boundaries or dislocations are eliminated by the grain growth after DRX. In addition, it should be noted that the grain structure is equiaxed and fairly uniform with straight grain boundaries. The structures of these grains are similar to those of statically recrystallized grains formed by nucleation and growth, but they are different from those of the dynamically recrystallized grains.[28] These microstructural features are associated with metadynamic recrystallization (MDRX). Thus, it is concluded that the present superalloy undergoes MDRX as well as DRX.

IV. CONCLUSIONS

The hot deformation behavior of the Co-33Ni-20Cr-10Mo superalloy with the fcc single-phase structure has been studied using compression tests at temperatures ranging from 950 °C to 1200 °C. The yield stress of the Co-33Ni-20Cr-10Mo superalloy is anomalous when compared to that observed in ordinary fcc alloys and is negative, and m is almost zero in the temperatures range of 950 °C to 1000 °C. This feature, which is caused by DSA, is associated with the high work-hardening characteristics of the alloy and deformation twinning during hot deformation.

Deformation twinning occurs during hot deformation in the temperature range of 950 °C to 1100 °C and contributes to the grain refinement of the dynamically recrystallized grains by providing nucleation sites at the

twin boundaries. The DRX occurs in the temperature range of 1000 °C to 1200 °C, and it depends on the strain rate; DRX tends to occur at high strain rates rather than at low strain rates. The yield drop phenomenon occurs at temperatures higher than 1100 °C, where DSA does not occur. The yield drop is caused by the unpinning of the residual dislocations that are immobilized by the solute molecules.

The small values of m at σ_{peak} and $\sigma_{0.5}$ at temperatures lower than 1050 °C suggest that the hot deformation mechanism at this temperature differs from that at temperatures higher than 1050 °C. The average Q values in the temperature range of 1100 °C to 1200 °C are 439 and 549.6 kJ/mol for σ_{peak} and $\sigma_{0.5}$, respectively. A linear relationship between In σ and In Z with regression coefficients of 0.99 to 0.98 is obtained in the aforementioned temperature range of 1100 °C to 1200 °C when using these Q values. High Q values ranging from 4484 to 1931 kJ/mole are obtained at temperatures lower than 1050 °C; this is because of the hot deformation associated with DSA or deformation twinning.

ACKNOWLEDGMENTS

REFERENCES

1. J.P. Immarigeon, K. Rajan, and W. Wallace: *Metall. Trans. A*, 1984, vol. 15A, pp. 339–45.
2. A. Chiba, X.G. Li, and M.S. Kim: *Philos. Mag.*, 1999, vol. 79, pp. 1533–54.
3. M.A. Meyers, O. Vohringer, and V.A. Lubarda: *Acta Mater.*, 2001, vol. 49, pp. 4025–39.
4. R.E. Reed Hill, J.P. Dieter, and H.C. Dieter: *Deformation Twinning*, Gordon and Breach, New York, 1964, p. 7.
5. P. Mullner, C. Solenthaler, and M.O. Speidel: *Acta Mater.*, 1994, vol. 42, pp. 1727–32.
6. G. Gottstein, H. Mecking, and D. Zabardjadi: *Proc. 4th Int. Conf. Strength of Metals and Alloys*, Nancy, France, 1976, pp. 1126–34.
7. R. Raj: *Trans. AIME*, 1981, vol. 12, pp. 1089–97.
8. C.E. Campbell, W.J. Boettinger, and U.R. Kattner: *Acta Mater.*, 2002, vol. 50, pp. 775–92.
9. H.J. McQueen and N.D. Ryan: *Mater. Sci. Eng.*, 2002, vol. 322, pp. 43–63.
10. M.C. Somani, K. Muraleedharan, Y.V.R.K. Prasad, and V. Singh: *Mater. Sci. Eng.*, 1998, vol. 245, pp. 88–99.
11. S.C. Medeiros, Y.V.R.K. Prasad, W.G. Frazier, and R. Srinivasan: *Mater. Sci. Eng.*, 2000, vol. 293, pp. 198–207.
12. A.A. Guimares and J.J. Jonas: *Metall. Trans. A*, 1981, vol. 12A, pp. 1655–66.
13. A. Kelly and R.B. Nicholson: *Progr. Mater. Sci.*, 1967, vol. 10, p. 984.
14. G.E. Dieter: *Mechanical Metallurgy*, 2nd ed., McGraw Hill Book Co., New York, NY, 1976, p. 138.
15. H. Monajati, M. Jahazi, S. Yue, and A.K. Taheri: *Metall. Mater. Trans. A*, 2005, vol. 36A, pp. 895–905.
16. R. Ebrahimi, A. Najafizadeh, and R. Shateri: *Proc. 81st Steel Symp.*, Iranian Institute for Iron and Steel, Isphahan, Iran, 2003, pp. 230–37.
17. A. Van Den Beukel and U.F. Kocks: *Acta Mater.*, 1982, vol. 30, pp. 1027–34.

18. F. Montheillet and J.J. Jonas: *Metall. Mater. Trans. A*, 1996, vol. 27A, pp. 3346–48.
19. T. Chunfeng, P. Feng, Q. Xuanhui, D. Baihua, W. Tianjian, and H. Xinbo: *Rare Met.*, 2008, vol. 27, pp. 292–98.
20. X. Yourong, C. Liangshen, J. Lei, and W. Deying: *Proc. 2nd Int. Conf.*, Intelligent Processing and Manufacturing of Materials, IPMM, Honolulu, 1999, vol. 2, pp. 805–10.
21. M.J. Weis, M.C. Mataya, S.W. Thompson, and D.K. Matlock: in *Superalloy 71- Metallurgy and Applications*, E.A. Loria, ed., TMS, Warrendale, PA, 1989, p. 135.
22. C.I. Garcia, G.D. Wang, D.E. Camus, E.A. Loria, and A.J. DeArdo: in *Superalloys 718, 625, 706 and Various Derivatives*, E.A. Loria, ed., TMS, Warrendale, PA, 1994, p. 293.
23. L.X. Zhou and T.N. Baker: *Mater. Sci. Eng.*, 1994, vol. A177, pp. 1–9.
24. W. Chen and M.C. Chaturvedi: *Mater. Sci. Eng.*, 1994, vol. A183, pp. 81–89.
25. S.C. Medeiros, Y.V.R.K. Prasad, W.G. Frazier, and R. Srinivasan: *Scripta Mater.*, 2000, vol. 42, pp. 17–23.
26. D.W. Livesey and C.M. Sellars: *Mater. Sci. Technol.*, 1985, vol. 1, pp. 136–44.
27. G. Shen, S.L. Semiatin, and R. Shivpuri: *Metall. Mater. Trans. A*, 1995, vol. 26A, pp. 1795–1803.
28. T. Sakai and M. Ohashi: *Mater. Sci. Technol.*, 1990, vol. 6, pp. 1251–57.